Research Article

Weiling Zhang, Mengqiao Xu, Tianyu Yuan, Wenjing Li, Xiangjun Dai*, Zhongwei Zhang, Hai Yun, and Yanxia Wang

Dual-biprism-based single-camera high-speed 3D-digital image correlation for deformation measurement on sandwich structures under low velocity impact

https://doi.org/10.1515/rams-2023-0136
received February 28, 2023; accepted October 13, 2023

Abstract: Herein, a single-camera stereo digital image correlation (DIC) method is developed for dynamic deformation measurement, and a dual-biprism high-speed stereo camera system is proposed to capture surface images. Then, full-field displacement and strain distributions are obtained after correlation and differential calculation using the stereo-DIC algorithm. After a typical experiment is performed to verify the accuracy of the proposed system, full-field displacement and strain distributions of sandwich panels subjected to low-velocity impacts are determined. These results show that the proposed system is an efficient and convenient tool for dynamic deformation measurement.

Keywords: digital image correlation, single high-speed camera, dynamic measurement

1 Introduction

Sandwich structures have been widely used in the aerospace, civil engineering, and construction industries because of their high stiffness-to-weight and strength-to-weight ratios, favorable energy-absorbing capacity, and excellent heat resistance and sound insulation [1]. During establishment or in service in an engineering context, sandwich panels produce significant deformation or cracks and lose their original protective function under the impact of external objects [2]. Furthermore, the external and internal damages caused by the impacts can cause a sudden catastrophic failure due to the reduction of stiffness and strength of structures. Thus, it is important to implement deformation measurement and understand the mechanical behavior of the structures during impacts [3].

As a noncontact optical measurement technique, a digital image correlation (DIC) method is widely used to investigate the mechanical behavior and damage fracture of sandwich structures due to the advantages of environmental vulnerability, simple experimental setup, and specimen preparation, and wide range of measurement sensitivity and resolution [4,5]. To measure the 3D shape and deformation of objects, three-dimensional DIC (3D-DIC) was developed based on the principle of binocular stereo vision [6,7]. 3D-DIC has been widely used in multidisciplinary fields such as vibration monitoring [8], nondestructive testing [9], biomedical [10], and mechanical and microstructural characteristics [11,12]. In conjunction with high-speed cameras, 3D-DIC can be used for the dynamic deformation measurement. In recent years, high-speed 3D-DIC has been applied to study the mechanical properties of composite structures subjected to low-velocity impact (LVI). For example, some researchers used it to explore the failure mechanism of sandwich plate [13], the evolution of low-speed impact-damage of composite laminates [14], and the deformation/failure processes of hybrid lamina composites [15].

However, the traditional high-speed 3D-DIC measurement system composed of dual cameras has some limitations. For example, stringent synchronization of the two cameras is required, particularly when they are applied to high-speed measurements. Moreover, the system has high hardware costs. Furthermore, some regions cannot

* **Corresponding author: Xiangjun Dai,** School of Transportation and Vehicle Engineering, Shandong University of Technology, Zibo 255049, China, e-mail: daixiangjun@sdut.edu.cn, tel: +86 533 278 6985
Weiling Zhang, Mengqiao Xu, Zhongwei Zhang, Hai Yun, Yanxia Wang: School of Transportation and Vehicle Engineering, Shandong University of Technology, Zibo 255049, China
Tianyu Yuan: Department of Engineering Mechanics, Southeast University, Nanjing 210096, China
Wenjing Li: School of Resources, Environment and Materials, Guangxi University, Nanning 530004, China

Open Access. © 2023 the author(s), published by De Gruyter. This work is licensed under the Creative Commons Attribution 4.0 International License.

be determined when applying the system to objects in a narrow area because the baseline length between the two cameras is insufficient in such areas. To overcome the disadvantage of synchronization, researchers have developed various single-camera 3D-DIC methods, such as diffraction-based [16], mirror-assisted [17,18], prism-based [19,20], and illumination source-based techniques [21,22]. Most of these systems were always limited to quasi-static deformation measurements in our knowledge.

In this study, a dual-biprism-based single-camera 3D DIC system was proposed for the high-speed deformation measurement. On the basis of the dual biprism stereo camera 3D DIC method mentioned in a previous study, we aim to investigate the feasibility and practicality of this technique for dynamic deformation measurements. A single high-speed camera was used to capture the surface images of honeycomb sandwich panels subjected to LVI. Subsequently, the full-field displacement and strain distributions were obtained after correlation and differential calculation using the stereo-DIC algorithm.

2 Methodology and system

2.1 Dual-biprism-based DIC

Figure 1 shows a schematic of the dual-biprism-based single-camera dynamic (DSD) DIC system, which consists of a high-speed camera, two biprisms, and a mirror. The biprisms were placed symmetrically on both sides of the optical axis of the camera, and the bases were fitted at a certain angle. When the specimen was placed at an appropriate distance in front of the biprism system, the left and right halves of the camera sensor could be imaged equally. The obtained subimages were equivalent to the specimen images obtained from different perspectives using two virtual cameras, as shown in Figure 2. According to the optical geometric model of the biprism [9], the imaging coordinate matrix of the system can be expressed as follows:

$$\begin{bmatrix} X_M \\ Y_M \\ Z_M \end{bmatrix} = \begin{bmatrix} 1 + K_1 \cdot \cos(\pi/4 + \alpha) & 0 & -K_1 \cdot \sin(\pi/4 + \alpha) \\ 0 & 1 & 0 \\ 1 - K_1 \cdot \cos(\pi/4 + \alpha) & 0 & K_1 \cdot \sin(\pi/4 + \alpha) \end{bmatrix}^{-1} \cdot \begin{bmatrix} -\zeta x_{m^+} - \left(\frac{L_B\sqrt{2}}{2} - L_L\right) \cdot K_2 \\ -\frac{\zeta}{2} \cdot (y_{m^+} + y_{m^-}) \\ -\zeta x_{m^-} - \left(\frac{L_B\sqrt{2}}{2} + L_L\right) \cdot K_2 \end{bmatrix}, \tag{1}$$

where X_M, Y_M, and Z_M are the coordinates of an object point M; x_{m^+}, y_{m^+} and $x_{m^-}y_{m^-}$ are the coordinates of image points m^+ and m^-, respectively; ζ is the corresponding magnification of the imaging system; L_B is the length of the biprism hypotenuse; L_L is the distance between the biprism and the lens; and α is the angle s the angle between the base of the biprism and the Z axis.

$$K_1 = \frac{\kappa}{\sqrt{1-\kappa}} - \sqrt{\kappa} \cdot \tan(\pi/4 + \alpha);$$

$$K_2 = \left[1 - \frac{\kappa}{\sqrt{1-\kappa} \cdot \cos(\pi/4 + \alpha)}\right] \cdot \sin(\pi/4 + \alpha);$$

and

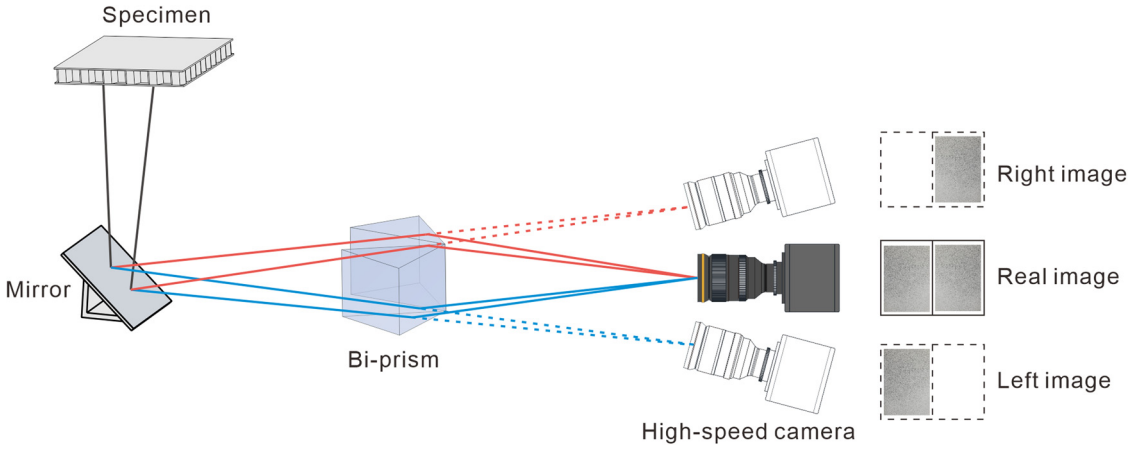

Figure 1: Schematic of the dual-biprism-based single-camera dynamic DIC system.

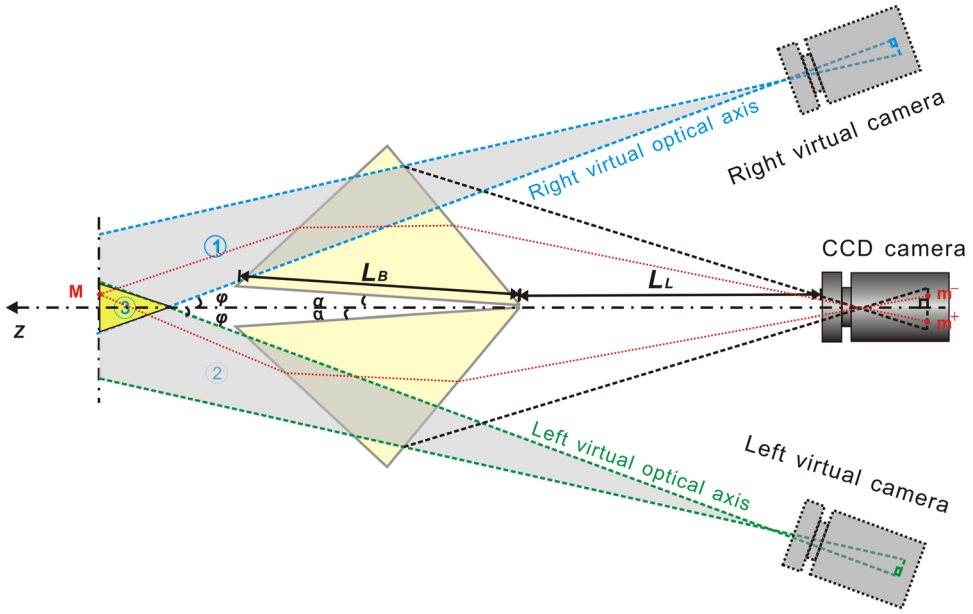

Figure 2: FOV of the proposed system.

$$\kappa = n^2 - \cos^2(\pi/4 + \alpha).$$

The field of view (FOV) can be changed by adjusting the angle between the two prisms or the position between the two prisms and camera. According to the virtual camera theory, there are two virtual optical axes. We assume that the FOVs of the right and left virtual cameras are represented by regions 1 and 2, respectively. The overlap of regions 1 and 2, as indicated by the yellow area, is the common observation field of the proposed system. As shown in Figure 2, the FOV can be expressed as follows:

$$-\varphi \le \text{FOV} \le \varphi, \tag{2}$$

where φ is the deviation and can be calculated from the following equation.

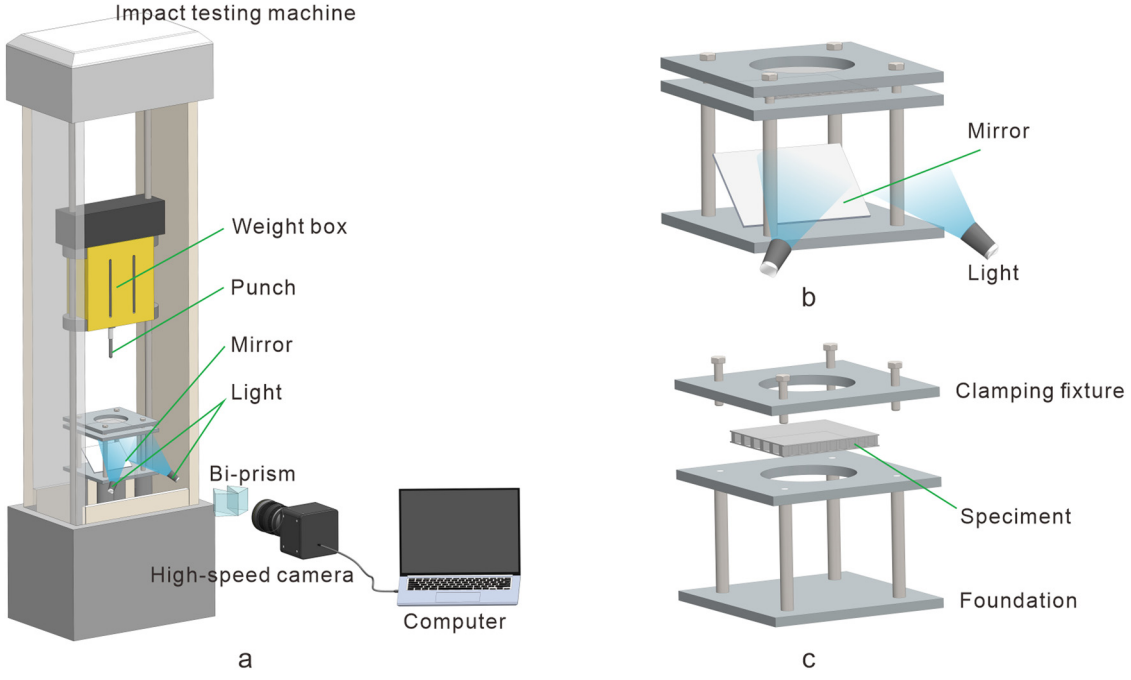

Figure 3: (a) Schematic of the experimental system for LVI, (b) mirror reflection system, and (c) test fixture.

$$\varphi = \arcsin\left(\sqrt{\frac{\Gamma^2(n^2-1) - \Gamma n^2 \sin\alpha - \sqrt{2}\Gamma \sin\left(\alpha - \frac{\pi}{4}\right) + n^2 - \sin^2\left(\alpha - \frac{\pi}{4}\right)}{\Gamma^2 + \Gamma \sin\alpha + 1}}\right) - \frac{\pi}{4} - \alpha, \tag{3}$$

where $\Gamma = \frac{L_B}{L_L}$, and n is the refractive index of the bi-prism.

2.2 Experimental set-up

Figure 3 shows a schematic of the experimental setup for the dynamic deformation measurement of the specimen subjected to LVI. The system consists of two parts: the proposed dual-biprism-based single-camera dynamic DIC system and the LVI test platform. A high-speed camera with 1,024 × 1,024 pixels and 6,400 full frame rate (Fastcam Mini AX200, PHOTRON Co., Ltd.) was used to record the deformation processing. To reduce the measurement error caused by external vibration, the DIC system was placed on an isolation platform composed of a cement base and a rubber base. During the experiment, a mirror reflection system was set up to record the images by the high-speed camera. The mirror was fixed in an inclined support with an angle of 45° to the horizontal direction. Two cold light sources were used to illuminate the nonimpact surface of the specimen, and the camera was focused on the nonimpact surface through the reflection of the mirror to perform the deformation measurement.

2.3 Experimental procedure

Figure 4 shows the experimental procedure used to determine the full-field deformation using the proposed method.

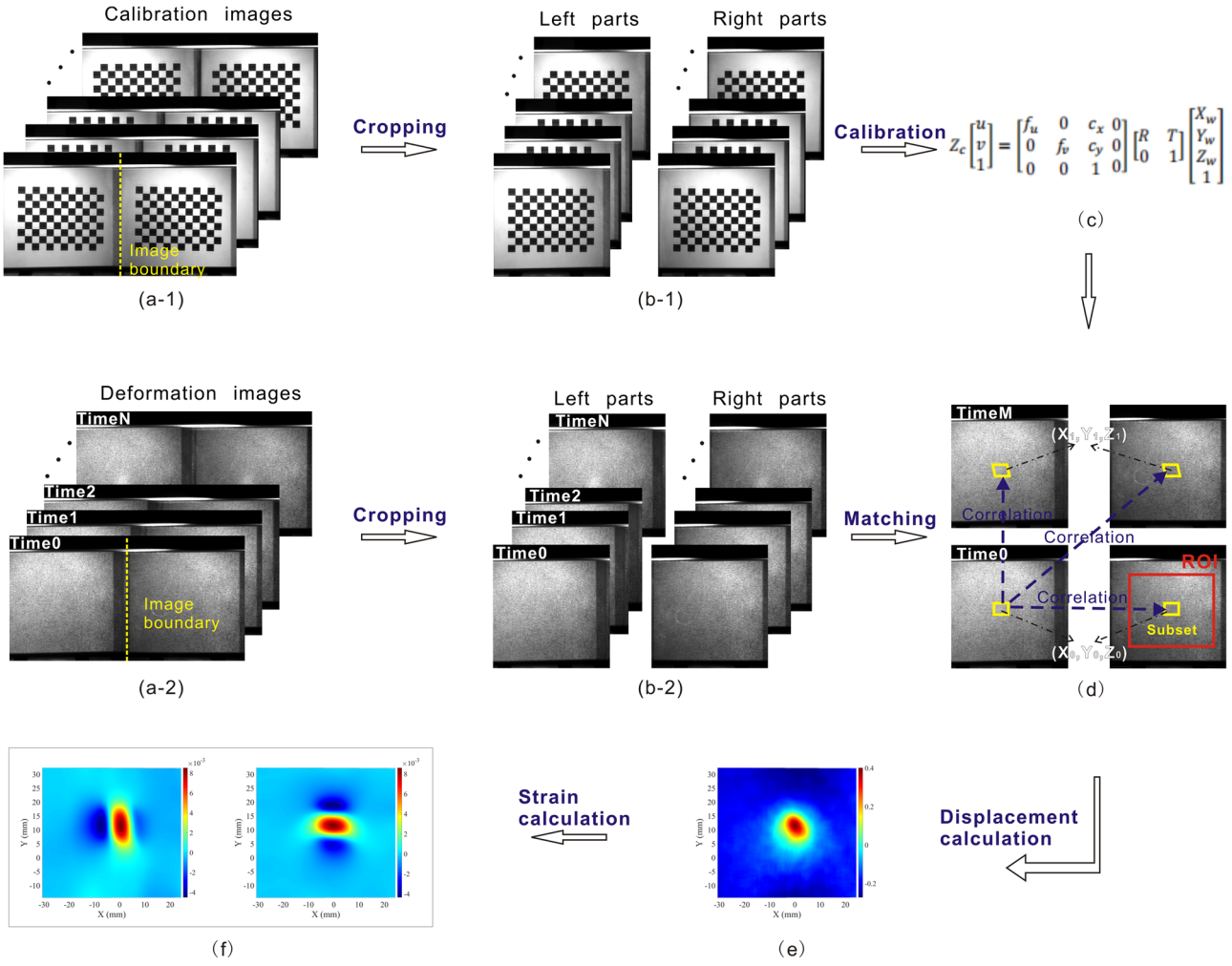

Figure 4: Main experimental procedure of dual-biprism-based DIC. (a-1) calibration images, (a-2) deformtion images, (b-1) cropped calibation images, (b-2) cropped deformation images, (c) coordinate transformation, (d) matching strategy, (e) displacement distribution, and (f) strain distribution.

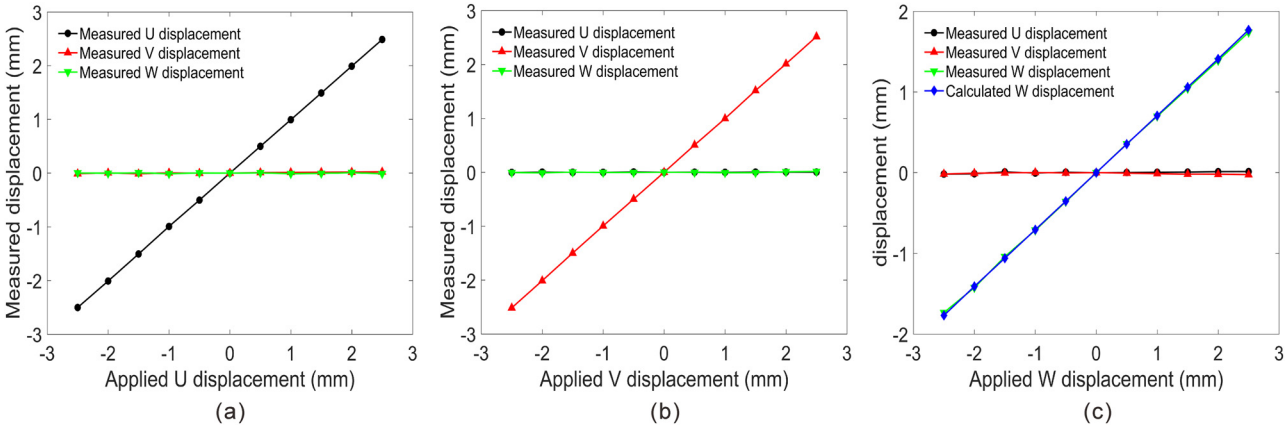

Figure 5: Relationship between applied and measured displacements: (a) *x* direction, (b) *y* direction, and (c) *z* direction.

The first step involved image acquisition. A series of calibration and surface images of the specimen were recorded using the DSD system. For the surface images, one undeformed image was captured as a reference and the others were targets. The second step involved image cropping. When a biprism pair was placed in front of the camera, the sensor was split into two halves. Subsequently, one image was split into two equal subimages. Hence, the coupled images were cropped along the perspective boundaries, as indicated by the dotted yellow lines in Figure 4(a-1) and (a-2). The corresponding subimage pairs are shown in Figure 4(b-1) and (b-2). Calibration was performed to obtain the intrinsic and extrinsic parameters of camera. 3D shape reconstruction and displacement calculations can be achieved by performing stereo matching. In this study, the matching strategy illustrated in Figure 4(d) was applied owing to the lack of incremental correlation and error accumulation and better robustness. After determining displacement, the full-field strain distributions were obtained using different algorithms [23,24]. The iterative least-square method was used in this research.

3 Experimental verification

To verify the accuracy of the proposed system, in-plane and out-of-plane displacements were measured and compared with the applied data. The calibration board was placed on the support, and the virtual images reflected by the plane mirror can be observed *via* the DSD system for calibration and displacement measurement. Figure 5 shows the schematic of the validation experiment. The two biprisms had the same optical parameters and sizes, with a refractive index of 1.5163 and a wedge angle of 45°. The plate used in the validation experiment was sized 100 mm × 100 mm × 1 mm, and the surface was sprayed with a random speckle. In-plane and out-of-plane translations were achieved using a 3D translation platform with an accuracy of 10 μm. During testing, the plate was fixed to the translation table, moving from −2.5 to −2.5 mm along the *x*, *y*, and *z* directions.

Figure 5(a)–(c) represent the relationship between 3D displacement and the applied displacement measured along the *x*, *y*, and *z* directions, respectively. As shown in the figure, displacement occurred only along the axial direction of the movement, whereas almost no displacement occurred along other directions. Figure 6 shows the standard deviation of the different applied displacements along the three directions. The figure shows that the error increased with the translation distance. Furthermore, the standard deviation of the out-of-plane displacement was

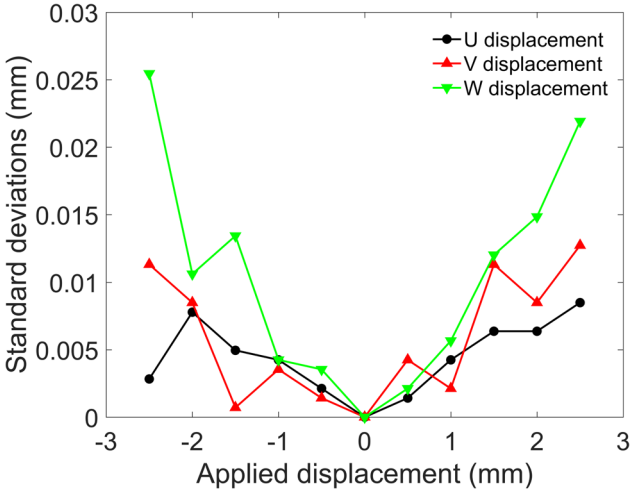

Figure 6: Standard deviations of different applied displacements.

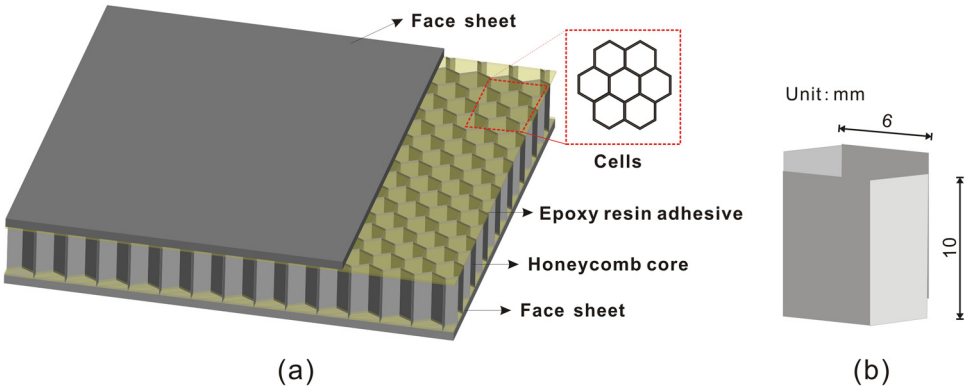

Figure 7: (a) Schematic diagram of structure of honeycomb sandwich plate and (b) dimension of cell.

slightly greater than that of in-plane displacement, but all values were less than 30 μm. Therefore, the measurement accuracy of the entire system is relatively high.

4 Application on sandwich plates

4.1 Materials

The proposed system was also applied on sandwich panels subjected to LVI. The face sheets and honeycomb core were made of aluminum and glued with an epoxy resin adhesive, as shown in Figure 7. The constituents of this alloy are listed in Table 1, and the mechanical properties of the honeycomb core and panel materials are listed in Table 2. The cell was a single layer of a positive hexagonal honeycomb with a length, thickness, and height of 6, 0.05, and 10 mm, respectively. The thickness of the front and rear panels was 0.5 mm, and the total thickness of the honeycomb sandwich structure was 11 mm. The honeycomb sandwich plates were cut into 100 mm × 100 mm before testing.

Table 1: Global chemical composition of aluminum alloy

Element	Al	Si	Fe	Cu	Mn	Mg	Zn	Ti	Other
wt%	99.18	0.25	0.35	0.05	0.03	0.03	0.05	0.03	0.03

4.2 Results and discussion

Both the single and repeated LVI tests were performed using a drop-weight impact machine with a 12-mm diameter hemispherical impactor according to the ASTM-D7136/D7136 M standard. The total mass of the impactor was 2.7 kg, and the maximum falling height of the setup was 2.0 m. The proposed optical system was used to record the deformation of the rear panels of sandwich structures.

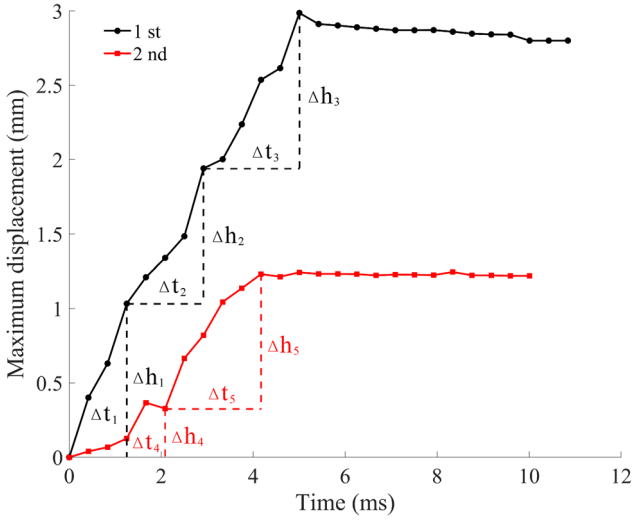

Figure 8: Maximum displacement–time histories for sandwich structure after LVIs.

Table 2: Mechanical properties of honeycomb core and panel materials

	Young's modulus of elasticity (GPa)	Poisson's ratio	Density (g·cm^{-3})
Honeycomb core	68	0.32	2.70
Panel	70	0.34	2.71

After calculating the displacement following the procedure mentioned earlier, the maximum displacement of the rear panel can be obtained.

Figure 8 shows the maximum displacement–time histories of the sandwich structure after LVIs. As is well known, the maximum displacement of the first impact at the same time is always greater than that of the second impact. The rate of shift change under the first impact was greater than that under the second impact, but the peak force arrived later. In addition, for the first impact, the maximum displacement tends to fall after the peak point, which indicates that there is a strain energy release and deformation rebound stage, and the sample still has impact-resistance and energy absorption properties. In contrast, although the second shock reached the peak displacement earlier, the maximum displacement was only 28% that of the first. In the unloading stage of the second impact, the specimen did not undergo significant displacement decline but exhibited a relatively flat fluctuation, which indicates that the specimen did not release energy on the observation surface. When the intact sample experienced the first impact, accompanied by collapse of the impact surface, compaction of the honeycomb core, and deformation of the nonimpact surface, the resistance to the impact force prolonged the entire loading process time.

For the first impact with a monotonically increasing displacement, the course of the first impact can be divided into segments t_1, t_2, and t_3 based on the time required for the same displacement obtained by deformation. As the displacement increases by t_1, t_2, and t_3 gradually increase,

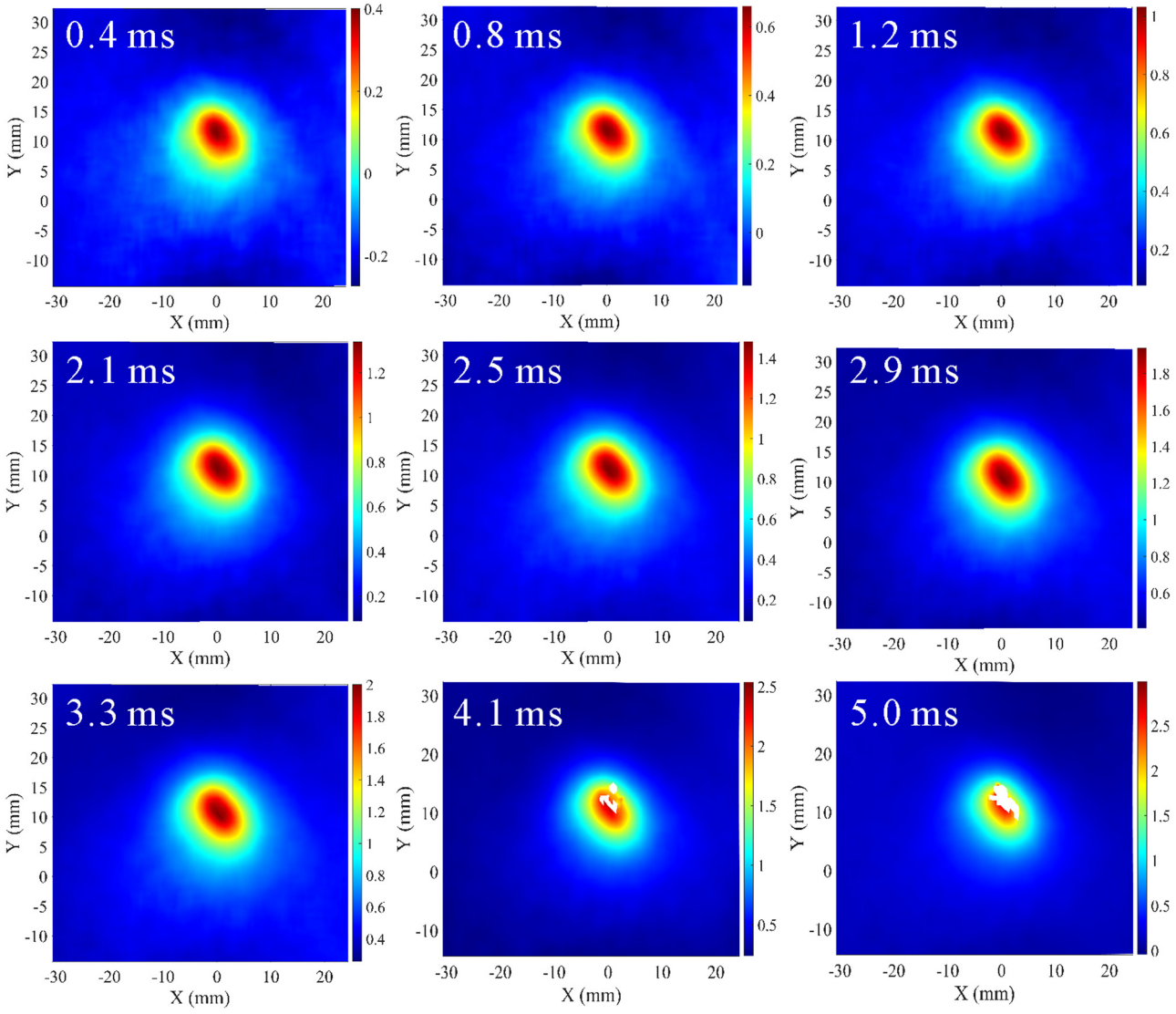

Figure 9: Typical out-of-plane displacements of the structure subjected to the first LVI at different times.

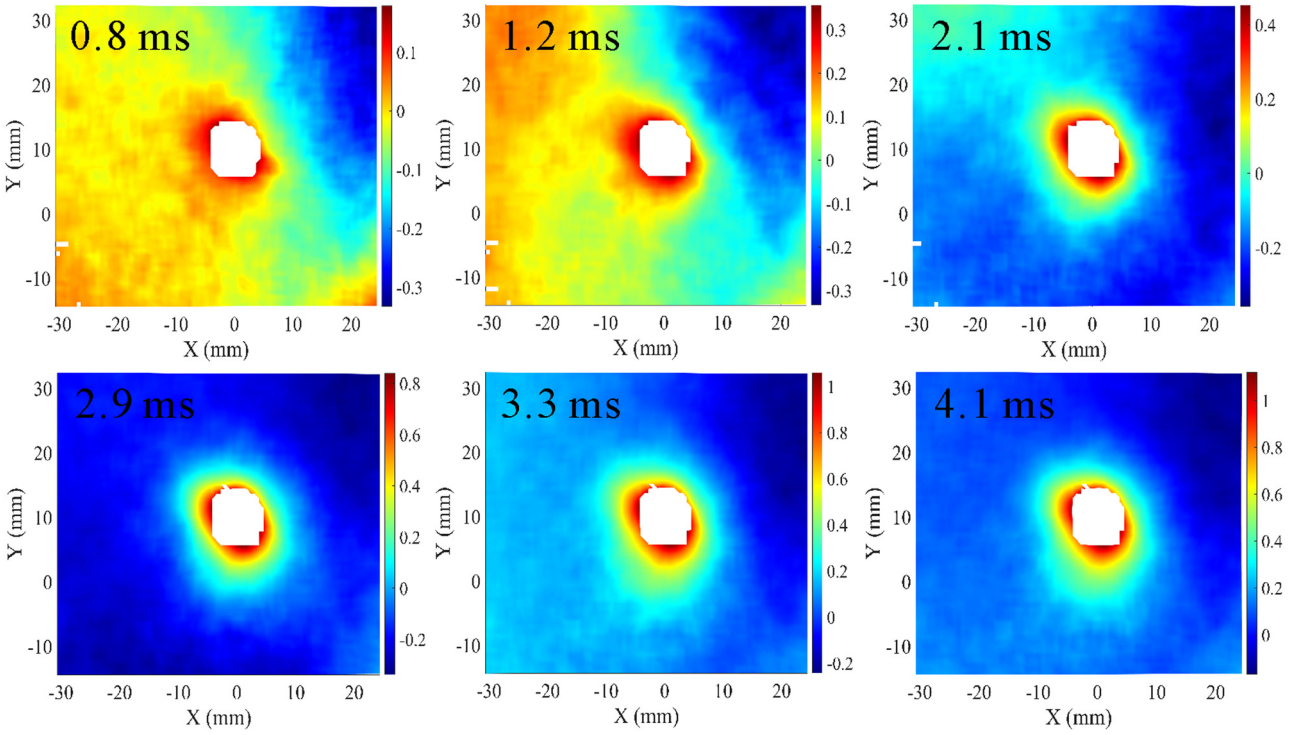

Figure 10: Typical out-of-plane displacements of the structure subjected to the second LVI at different times.

which indicates that the increment in impact deformation decreases.

For the first impact, the curve increases monotonically and sharply before the displacement reaches the maximum value of 2.98 mm. After the peak point, the curve decreases slowly. Three points on the displacement–time curve were used to mark three different stages for the first impact history of the sandwich plate as shown in Figure 8. Starting from the reference, the time elapsed for each segment was t_1, t_2, and t_3, corresponding to the range of changes in the maximum displacement values of Δh_1, Δh_2, and Δh_3, respectively. Although three changes in the

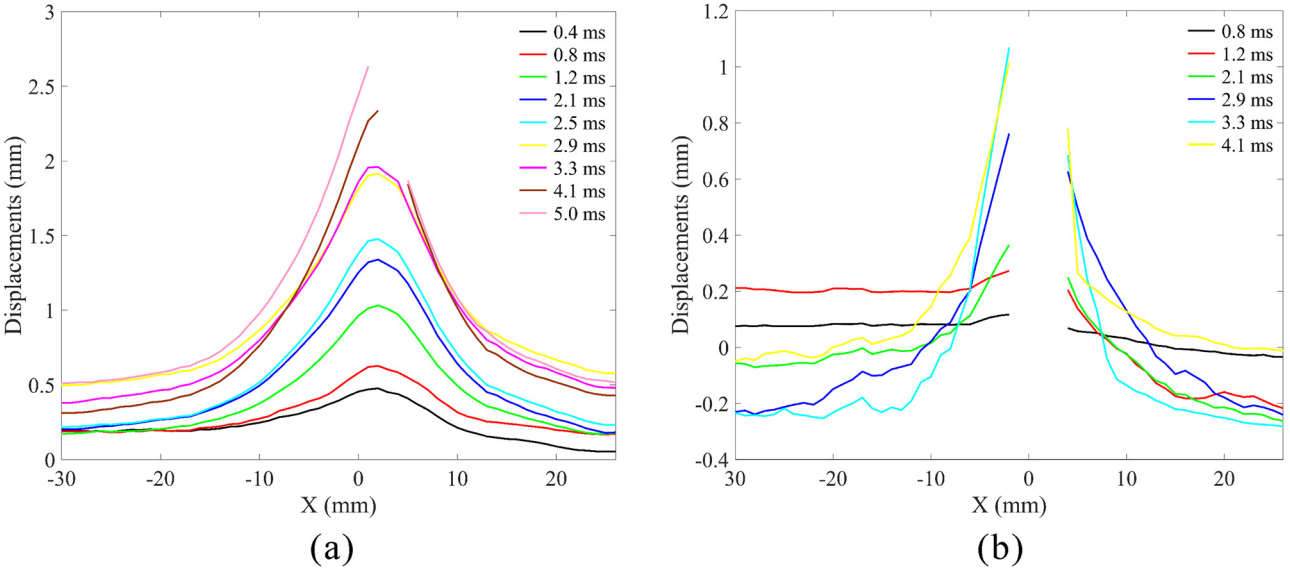

Figure 11: Out-of-plane displacements distributions along the cross section: (a) first impact and (b) second impact.

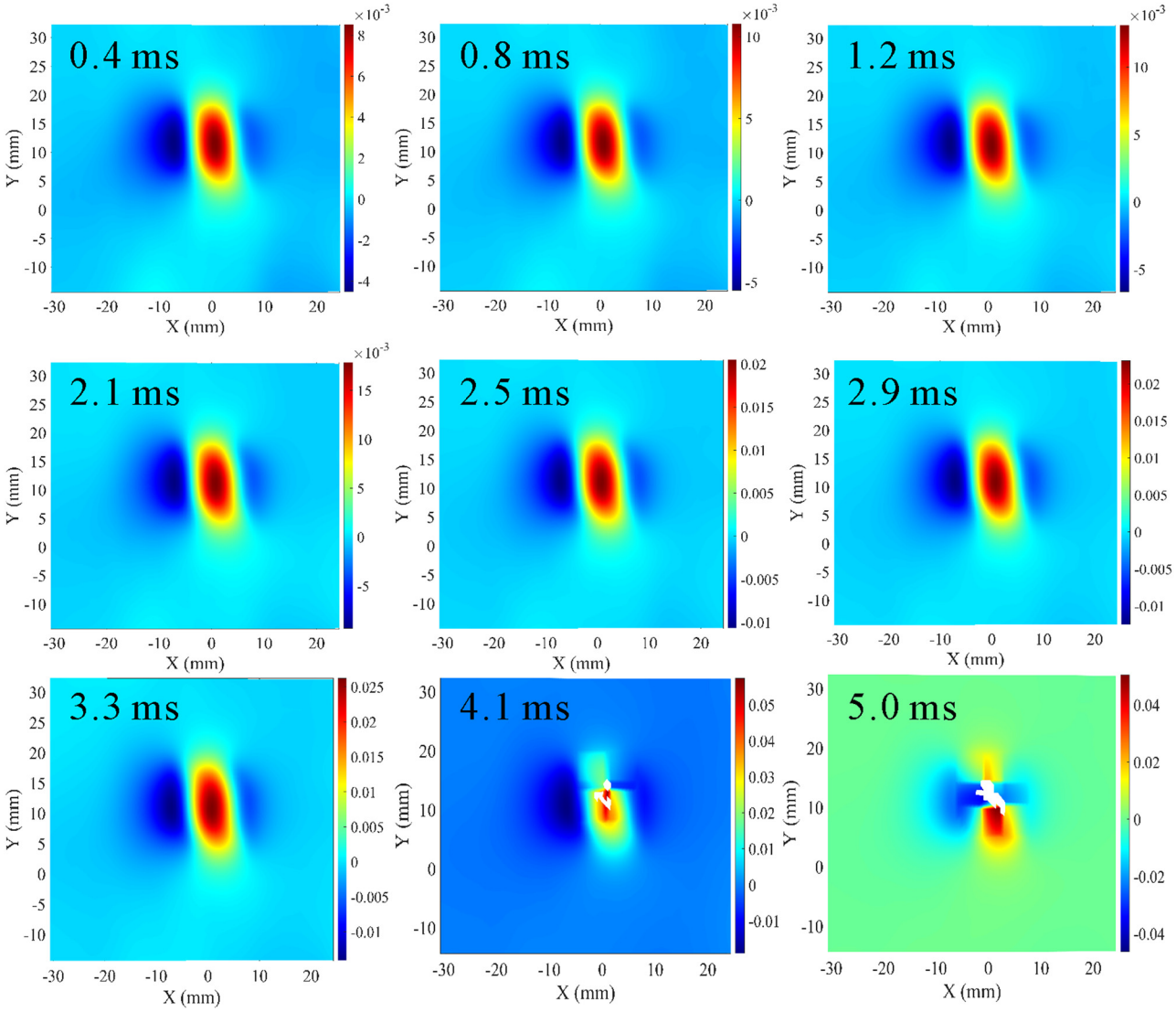

Figure 12: Normal strain in the *x* direction for the first LVI at different times.

maximum displacement increment were experienced, the time required gradually increased. Further, the increment of the maximum displacement value decreased, while the value of the maximum slope experienced in each time decreased. It indicates that LVI led to severe internal and external damage such that the impact resistance was reduced. During the process, the stiffness of the sandwich structure decreased gradually. Furthermore, the upper sheet failed and the honeycomb cores became more dense.

Similarly, the second impact can be divided into t_4 and t_5 stages. Notably, t_4 and t_5 represent displacement fluctuation segments with a steady rising phase. The maximum displacement increments are Δh_4 and Δh_5, respectively. Under the second impact, the deformation increment during t_5 is much greater than that in t_4, which may be due to the full penetration of the nonimpacted surface. After the peak value of 1.23 mm, the displacement is almost invariant because of the puncture failure of the rear face sheet.

Figures 9 and 10 show the out-of-plane displacement distributions of the observed surfaces at typical moments during the first and second LVIs, respectively. When no visual damage occurred on the observation surface, the deformation was mainly concentrated at the impact position as an ellipse and spread. As shown in Figure 9, with the increasing impact force, the overall displacement of the observation surface increased, thereby resulting in a more concentrated trend when the specimen was subjected to the first LVI. At 4.1 ms, the observation surface was damaged, which is the reason for the sudden drop in the slope, as shown in Figure 8. Subsequently, the damage area gradually expanded.

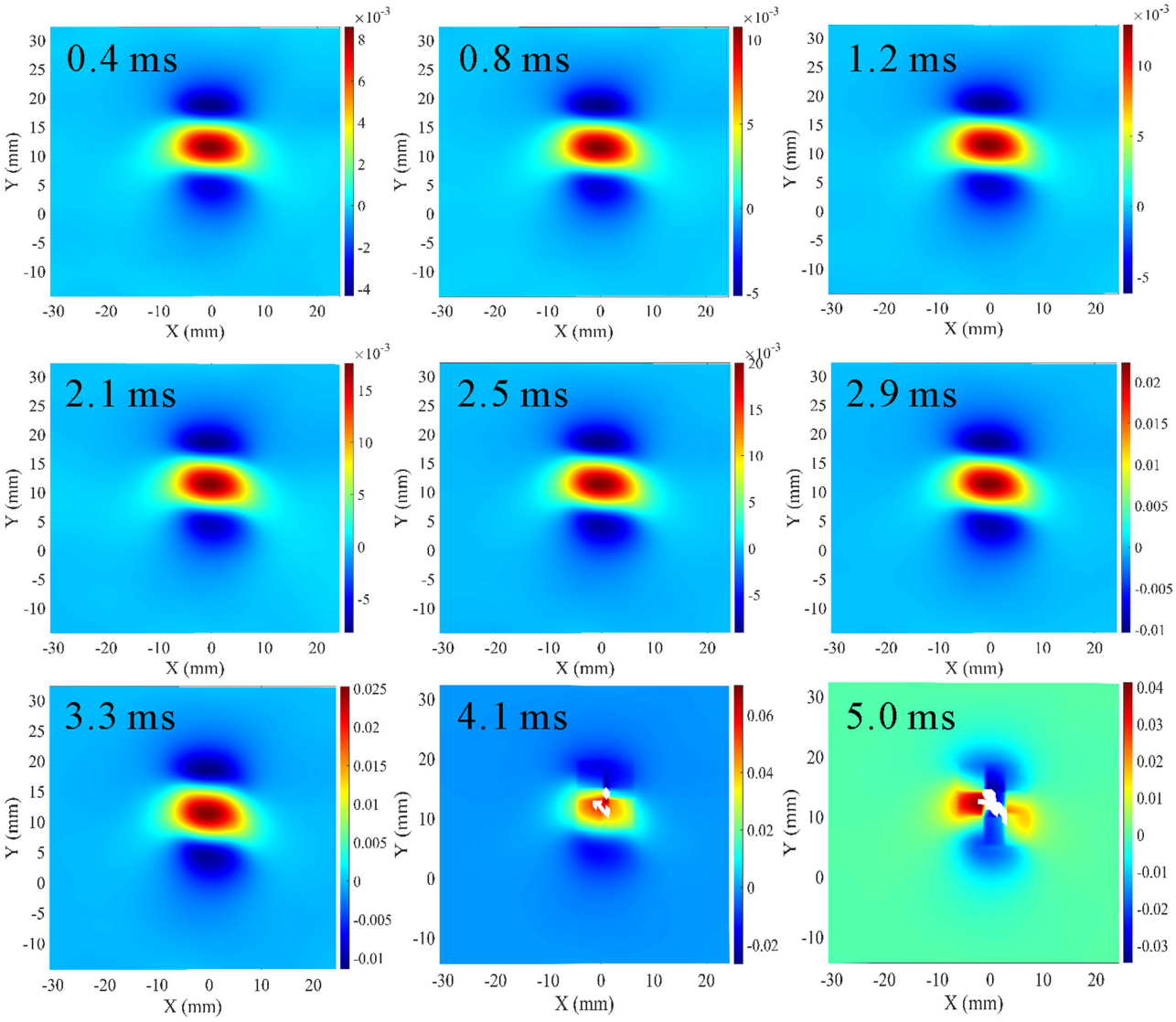

Figure 13: Normal strain in *y* direction for the first LVI at different times.

When the structure was under the second LVI, the region adjacent to the impact center deviated less from the impact center, although the maximum displacement was still concentrated near the impact center. The deformation increment decreased significantly, which was caused primarily by the collapse and fracture of the honeycomb core material absorbing the impact and limited panel bearing force. It can also be found in Figures 9 and 10 that the damage area increased with impact time for the first LVI, while it did not increase significantly for the second LVI. The reason is that the honeycomb core improved the damage resistance as it helped in absorbing the impact energy during the impact. Most of the energy was absorbed and dispersed by transferring it to the adjacent honeycomb core, reducing the likelihood of puncture failure of the rear panel in the first impact. As for the second impact, the panels and core were broken at the initial state, and there was little damage expansion after penetration.

Figure 11 shows a comparison of the out-of-plane displacement distributions along the cross-section. The displacement of the first impact exhibited a good symmetrical distribution. Under the loading of the punch, the right side of the impact center cracked first until the end of the first LVI, and the maximum cracking width reached 6.4 mm. It should be noted that the crack position was random and influenced by many factors, such as the flatness, support, collimation of the impact, and integrity of the internal structure. For the second LVI, the distribution of displacement exhibited good symmetry only after 2.1 ms. The width of the region adjacent to the impact center changed less after the specimen was penetrated.

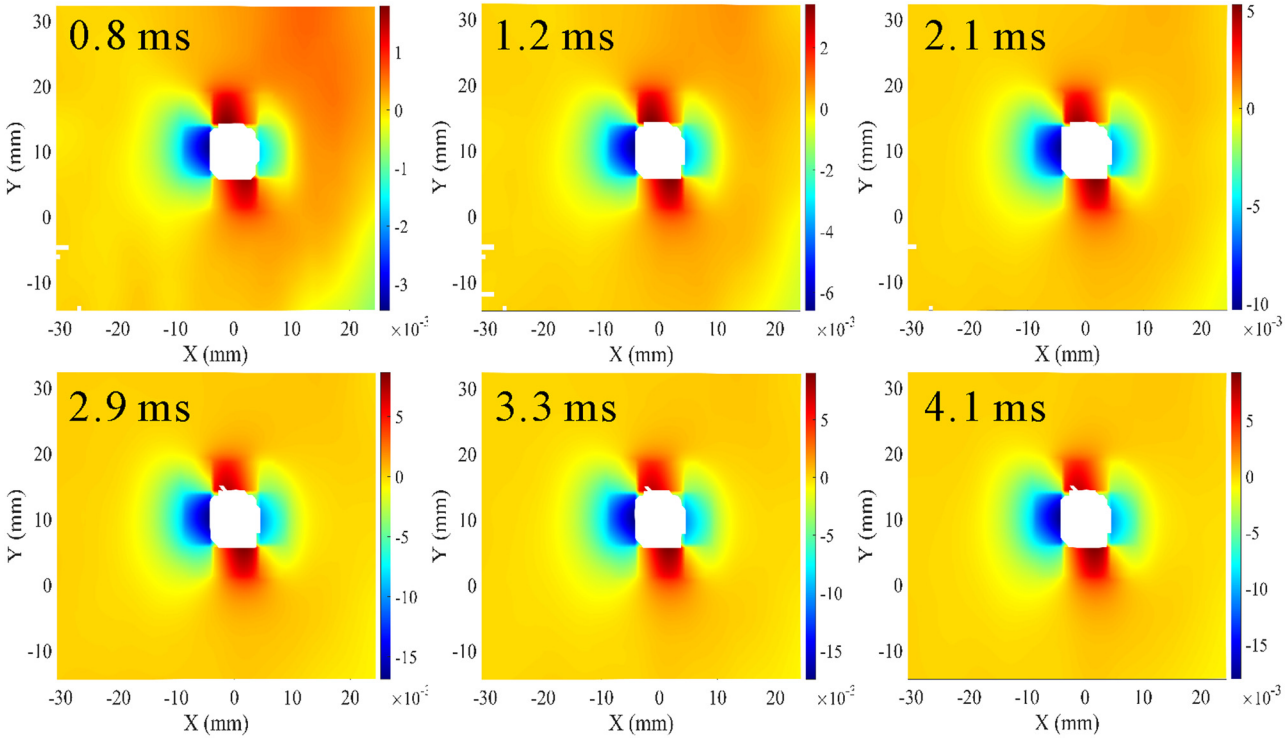

Figure 14: Normal strain in the *x* direction for the second LVI at different times.

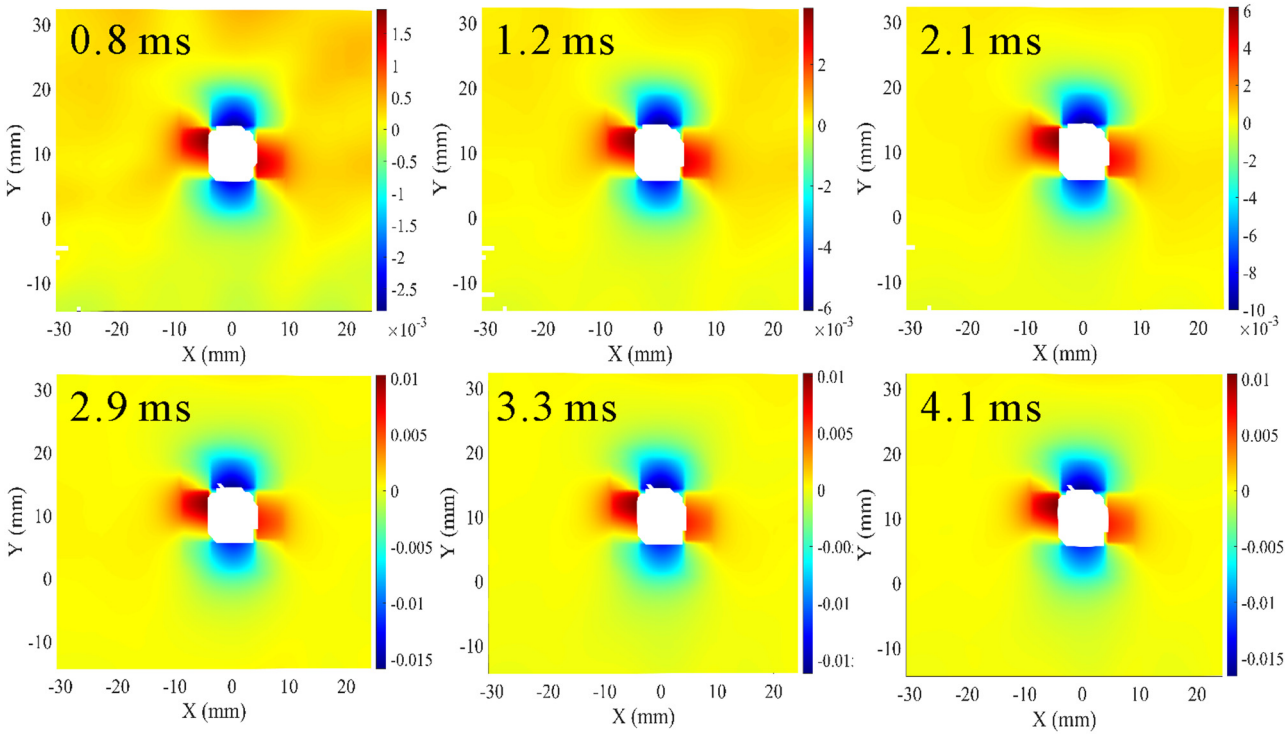

Figure 15: Normal strain in the *y* direction for the second LVI at different times.

The full-field strain distributions of the sandwich structure were obtained based on the strain calculation algorithm. Figures 12 and 13 show the normal strains in the x and y directions for the first LVI at different times. The figures show that the strain concentration occurred primarily around the impact regions. The strain magnitudes increased as LVI proceeded. Moreover, the closer it is to the impact center, the greater the change in amplitude. In contrast, the strain in the area away from the impact center was smaller and had no significant fluctuations during impact processing. The normal strain in the x direction was presented as a vertically symmetrical butterfly shape except at 5 ms. This is because the areas located on the left and right sides were under compression, whereas the impact regions were in a state of tension. A similar distribution was also observed in the normal strain in the y direction.

Figures 14 and 15 show the normal strains in the x and y directions for the second LVI at different times. As in the first impact, the strain magnitudes increased as the LVI proceeded, and the change in the amplitude was great closer to the impact center. However, the difference is that the strain no longer exhibited a butterfly-shaped distribution, but a flower-shaped distribution. Moreover, there are compressive and tensile areas around the impact point with a symmetrical distribution. In particular, the loading affected the core materials and panels around the impact area, although the panels were punched through. Then, a clear strain distribution around the impact region and fluctuations in the far-field are observed. This fluctuation faded with the impact time. It indicates that, during the impact, most of the energy was absorbed by the honeycomb core and panels near the impact center, causing severe plastic deformation, fragmentation, and buckling in the first LVI. As for the second impact, the impact energy spread out along the horizontal direction and reached the edges, while the energy transfer was slow in the vertical direction.

5 Conclusion

In this study, a dual-biprism-based single-high-speed camera stereo DIC system was developed for dynamic deformation measurement. The system comprises two biprisms, one reflection mirror, and a single high-speed camera, which makes it low cost and easy to implement and maintain. Moreover, it overcomes the synchronization issue associated with the use of two high-speed cameras. The effectiveness and accuracy of the system were verified using in-plane and out-of-plane displacement experiments.

The proposed system was used to investigate the full-field displacement and strain distributions of honeycomb sandwich panels subjected to LVI. For both the first and second LVIs, the overall displacement of the observation surface increased with the increasing impact force, thus leading to a more concentrated trend. For the first LVI, the strain magnitudes increased as the LVI proceeded. Furthermore, the change in amplitude was closer to the impact center. The normal strains in the x and y directions were presented as vertically symmetrical butterfly shapes, except at 5 ms. For the second LVI, the normal strains in the x and y directions were flower shaped owing to the compressive and tensile stresses around the impact center.

Although the proposed DSD DIC system achieved a good performance on determining the surface deformation of sandwich structures during the impacts in the current research. It has its own limitation of the loss of the spatial resolution as the CCD sensor was split into two halves to capture the stereo views. Further research on the developed system without resolution loss can be expected. Moreover, it is worth studying how to use the real-time displacement and strain field information for the design or property-enhancement of the materials in the future.

Acknowledgments: The authors thank the anonymous reviewers for their fruitful suggestions to improve the article.

Funding information: This work was supported by the National Natural Science Foundation of China (Nos. 12172200 and 11672167).

Author contributions: All authors have accepted responsibility for the entire content of this manuscript and approved its submission.

Conflict of interest: The authors state no conflict of interest.

References

[1] Dai, X., H. Ye, W. Yang, J. Qi, Y. Liu, T. Yuan, et al. Mechanical behaviors of inner and outer sidewalls of honeycomb cores subjected to out-of-plane compression. *Aerospace Science and Technology*, Vol. 127, 2022, id. 107659.

[2] Ahmad, S. I., H. Hamoudi, A. Abdala, Z. K. Ghouri, and K. M. Youssef. Graphene-reinforced bulk metal matrix composites: synthesis, microstructure, and properties. *Reviews on Advanced Materials Science*, Vol. 59, No. 1, 2020, pp. 67–114.

[3] Chen, Z., Y. Zhang, J. Wang, G. Hota, R. Liang, Y. Zhang, et al. Experimental and modeling investigations of the behaviors of syntactic foam sandwich panels with lattice webs under crushing loads. *Reviews on Advanced Materials Science*, Vol. 60, No. 1, 2021, pp. 450–465.

[4] Dai, X., T. Yuan, Z. Zu, H. Ye, X. Cheng, and F. Yang. Experimental investigation on the response and residual compressive property of honeycomb sandwich structures under single and repeated low velocity impacts. *Materials Today Communications*, Vol. 25, No. 1, 2020, id. 101309.

[5] Ye, H., X. Dai, T. Yuan, J. Zhou, J. Zhang, and S. Shao. Residual compression property and response of honeycomb sandwich structures subjected to single and repeated quasi-static indentation. *Reviews on Advanced Materials Science*, Vol. 60, No. 1, 2021, pp. 404–417.

[6] Su, Z., J. Pan, S. Zhang, S. Wu, Q. Yu, and D. Zhang. Characterizing dynamic deformation of marine propeller blades with stroboscopic stereo digital image correlation. *Mechanical Systems and Signal Processing*, Vol. 162, 2021, id. 108072.

[7] Su, Y., Z. Gao, H. Tu, Y. Wang, Y. Liu, Z. Fang, et al. Uniformity and isotropy of speckle pattern cause the doubled random error phenomenon in digital image correlation. *Optics and Lasers in Engineering*, Vol. 131, 2020, id. 106097.

[8] Wu, R., D. Zhang, Q. Yu, Y. Jiang, and D. Arola. Health monitoring of wind turbine blades in operation using three-dimensional digital image correlation. *Mechanical Systems and Signal Processing*, Vol. 130, 2019, pp. 470–483.

[9] Yuan, T., X. Dai, X. Shao, Z. Zu, X. Cheng, F. Yang, and X. He. Dual-biprism-based digital image correlation for defect detection of pipelines. *Optical Engineering*, Vol. 58, No. 1, 2019, id. 014107.

[10] Shao, X., X. Dai, Z. Chen, and X. He. Real-time 3D digital image correlation method and its application in human pulse monitoring. *Applied Optics*, Vol. 4, No. 55, 2016, id. 696.

[11] Zhao, Y. and Y. Gu. Deformation mechanisms and plasticity of ultrafine-grained Al under complex stress state revealed by digital image correlation technique. *Nanotechnology Reviews*, Vol. 10, No. 1, 2021, pp. 73–86.

[12] Zhong, X., Z. Bai, J. Wu, H. Long, H. Deng, Z. Chen, et al. Microstructural characteristics and nano-modification of interfacial transition zone in concrete: A review. *Nanotechnology Reviews*, Vol. 11, No. 1, 2022, pp. 2078–2100.

[13] Bai, R., J. Guo, Z. Lei, D. Liu, and C. Yan. Compression after impact behavior of composite foam-core sandwich panels. *Composite Structures*, Vol. 225, 2019, id. 111181.

[14] Tuo, H., Z. Lu, X. Ma, J. Xing, and C. Zhang. Damage and failure mechanism of thin composite laminates under low-velocity impact and compression-after-impact loading conditions. *Composites Part B: Engineering*, Vol. 163, 2019, pp. 642–654.

[15] Hao, X., T. Jin, X. Ma, X. Shu, and X. Li. Dynamic response of single curved fiber-metal hybrid lamina composites subject to low-velocity impact. *International Journal of Impact Engineering*, Vol. 164, 2022, id. 104209.

[16] Pan, B., L. Yu, and Q. Zhang. Review of single-camera stereo-digital image correlation techniques for full-field 3D shape and deformation measurement. *Science China-Technological Sciences*, Vol. 61, 2018, pp. 2–20.

[17] Wang, R., X. Li, and Y. Zhang. Analysis and optimization of the stereo-system with a four-mirror adapter. *Journal of the European Optical Society-Rapid Publications*, Vol. 3, 2008, id. 08033.

[18] Yu, L. and B. Pan. Structure parameter analysis and uncertainty evaluation for single-camera stereo-digital image correlation with a four-mirror adapter. *Applied Optics*, Vol. 55, 2016, pp. 6936–6946.

[19] Lim, K. B. and Y. Xiao. Virtual stereovision system: new understanding on single-lens stereovision using a biprism. *Journal of Electronic Imaging*, Vol. 14, 2005, id. 043020.

[20] Wu, L., J. Zhu, and H. Xie. A modified virtual point model of the 3D DIC technique using a single camera and a bi-prism. *Measurement Science & Technology*, Vol. 25, No. 11, 2014, id. 115008.

[21] Yu, L. and B. Pan. Color stereo-digital image correlation method using a single 3CCD color camera. *Experimental Mechanics*, Vol. 57, 2017, pp. 649–657.

[22] Li, J., X. Dan, W. Xu, Y. Wang, G. Yang, and L. Yang. 3D digital image correlation using single color camera pseudo-stereo system. *Optics and Laser Technology*, Vol. 95, 2017, pp. 1–7.

[23] Pan, B., K. Qian, H. Xie, and A. Asundi. Two-dimensional digital image correlation for in-plane displacement and strain measurement: a review. *Measurement Science and Technology*, Vol. 20, 2009, id. 062001.

[24] Dai, X., H. Ye, T. Yuan, X. Shao, Z. Zu, X. Cheng, et al. Strain determination based on strain gauge-guided radial basis function and digital image correlation. *Optics and Lasers in Engineering*, Vol. 126, 2020, id. 105894.